TECHNOLOGIES FOR
NEW INDIA@75
आज़ादी का अमृत महोत्सव

Technical Article

• First-Principles Study of Thermodynamic Properties of U with Point-Defects and of U-Pu and U-Zr Alloys

Young Officer's FORUM

• Synthesis of CVD Pyrolytic Graphite at Different Pyrolysis Temperature for Pyrochemical Reprocessing Application

Young Researcher's FORUM

• Resolving Isobaric interference and accurate measurement of Cs and Sr in the dissolver solution by using Isotopic Dilution Thermal Ionisation Mass Spectrometry (ID-TIMS)

News and Events

• Internal review meeting on 'Role of Defects in Condensed Matter- Vistas from Materials Science Group'

Awards, Honours and Recognitions

Bio-diversity @ DAE Campus, Kalpakkam

New Year 2023 Message

Dear Colleagues,

It is my pleasure to wish all colleagues of Indira Gandhi Centre for Atomic Research and General Services Organization and their near and dear ones a very joyous, healthy, blissful and prosperous New Year 2023.

Looking back, the year 2022 had definitely many milestone activities. To list some of them,

The Fast Breeder Test Reactor (FBTR) was raised to its rated design power level of 40 MWt for the first time on 7th March 2022. The reactor has operated for more than 128 days and generated more than 23.5 million Units during 2022. The U-233 based Kalpakkam Mini Reactor (KAMINI) continued to operate up to 30 kWt for neutron radiography of irradiated fuel pins, activation analysis of samples from AMD-Hyderabad, ASI, Institutions and testing of neutron detector etc.

As you would be aware, the Prototype Fast Breeder Reactor (PFBR) at BHAVINI is in an advanced stage of integrated commissioning. The entire design and also the Electronics and Instrumentation group is fully working with BHAVINI team for the various issues and activities. Focused support from other groups such as ESG and SQRMG is also being provided. Three major activities that have been successfully accomplished include (a) Baselining of more than 250 documents pertaining to V&V of I & C – pre requisite for Main Vessel Sodium Filling (b) rectification of 741 dummy subassemblies and (c) Successful demonstration of ISI vehicle DISHA.

COmpact Reprocessing facility for Advanced fuels in Lead shielded cells (CORAL), facility has successfully completed its 63rd campaign and is continuing to function normally well beyond its design intent. Demonstration fast reactor Fuel Reprocessing Plant (DFRP), has reached an advanced stage with the cold commissioning being successfully completed.

In our endeavour towards indigenous development of improved materials and processes, phase-pure, high-density (~99.8%) tungsten carbide pellets of diameter 13.4mm and height 9.1mm have been fabricated in-house using a spark plasma sintering facility, for use as lower axial shielding in FBTR fuel sub-assemblies Post-Irradiation Examination through NDE of irradiated fuel pins

from a FBTR Mark-I sub-assembly operated at a linear heat rate of 400 W/cm was completed. A multiple specimen test facility has been developed to study the crack growth behaviour of small-sized pipe bends. First phase of testing on specimens has been carried out.

Cadmium Zinc Telluride single crystals of size 5×5×5 mm have been grown in-house and also incorporated in to a gamma radiation detector and found to have adequate gamma ray spectral resolution and stability. Larger (~25mm) crystals have been grown and are undergoing tests. A high-resolution RBS system with depth resolution of 0.2-0.3nm has been applied to thickness and stoichiometry of ultra-thin film multi-layers. This has enabled correlation of interface features in Ni/Si/Ni/Si and Ni/Graphene/Ni/SiC with magneto-resistance measurements to demonstrate ferromagnetic coupling across silicon layers in the former case and antiferromagnetic coupling across graphene layers in the latter case.

As part of metal fuel development activities, U-6 wt. % Zr blanket slugs were fabricated using the upgraded injection casting system (10 kg) inside inert atmosphere glove box and was qualified for its functionality. Prior to electro-refining irradiated U-Zr alloy fuel, all the optimization process parameters were carried out utilizing virgin U-Zr alloy in molten salt medium at Hot-cells. Subsequently, uranium metal deposition was successfully demonstrated by electro-refining irradiated U-6Zr. In addition, an engineering scale pyroprocessing facility with remote handling has been established and electro-refining of 10 kg uranium metal was demonstrated in this facility.

An Integrated Radiation Monitoring Facility (IRMF) was commissioned at Anupuram Township and inaugurated by the then Chairman AERB Shri Nageswara Rao. A team from NDMA also visited the facility and appreciated it. First responder training course on Nuclear & Radiological Emergencies was conducted at IGCAR for 244 personnel from National Disaster Responses Force (NDRF), Arakkonam in six batches. More than 600 radiation monitoring equipments from various DAE units, hospitals, industries were calibrated at the NABL accredited Calibration facility.

During this period, two technologies developed under "Atma Nirbhar Bharat" programmes of IGCAR have been successfully transferred to industry through the Incubation Centre. Two Indian patents were granted. A collaborative incubation agreement was also signed with a Mumbai based private manufacturer to complete development of the technology "Replaceable Feed-through connectors for Glove Boxes" and Chennai based firm for developing "Hydrogen Sensor" technology.

Towards human resources development, twenty young trained scientists and engineers (OCES-2021, 16th Batch) have successfully completed their orientation programme at BARC Training School at IGCAR and were placed in various units of DAE. Our Centre has been providing projects/internship opportunity to Postgraduate students for completing their academic programme and thereby aids to kindle the interest in students to pursue research in frontier areas of science and technology.

As part of Azadi Ka Amrit Mahotsav celebrations a program an 'Anu Awareness' programme was organized. An exhibition depicting the role of nuclear energy, applications of radiation and DAE based technologies for society, quiz and other competitions were organized. More than 2000 students participated in the competitions and around 20,000 students, teachers and researchers visited the exhibition. 'Grand Iconic Week' was celebrated from August 22-28, 2022 as part of the 'Azadi Ka Amrit Mahotsav' on the theme 'Atoms in the Service of the Nation'. Generation of 750 Magic Squares" by 75 students from eight neighbourhood Govt. Higher Secondary Schools using 75 important dates of milestone activities of DAE, 'Sand art sculpture' by Artist Gajendran to create awareness on the societal applications of various technologies developed by DAE and 'Anu Walkathon' for ATOMS IN THE SERVICE OF THE NATION at Elliot's beach, Chennai were some of the highlights of the celebration.

Foundation Day was celebrated on 30th April 2022. The event was graced by Shri G. Nageswara Rao, the then Chairman, AERB, Dr. D. K Sinha, the then Director, AMD, Dr. P. R. Vasudeva Rao, the then Vice Chancellor, HBNI, Dr. Shankar V Nakhe, Director RRCAT, Indore, as also many former Directors and Group Directors. A document on the "Journey of FBTR- Reaching Further Heights", "a Booklet in Hindi on the "Activities of IGCAR "and book on "Butterflies of Kalpakkam" were released on Foundation Day.

The important dignitaries to visit the Centre during this year include – Dr. Anil Kakodkar, Chancellor HBNI, Member AEC and former Chairman AEC, Dr. Samir V Kamat, Chairman, DRDO & Secretary, Dept. of Defence R&D, New Delhi, Shri S. S. Bajaj, former Chairman AERB,

Dr. B. N. Suresh, Chancellor, IIST and former Director VSSC, Shri M. S. R. Prasad former DG (Missiles) and DRDO VS Chair, Shri S. A. Bhardwaj, former Chairman AERB, Dr. M. Rajeevan, Former Secretary (Earth Sciences), Vice Admiral S. P. S. Cheema,

Dr. R. Venugopal, Joint Chief Controller of Explosives, Vadodara Circle, Gujarat, Dr. M. Sai Baba, Director, CPD&T, M.S. Ramaiah University and Shri Manoj Kumar Lal, DGP Puducherry.

General Services Organisation continues to efficiently maintain the residential and infrastructural buildings. GSO has completed the construction of four tower blocks and the efforts put in by employees of GSO in maintaining the townships serene, green and clean is commendable. The Medical Group has provided good services to the CHSS beneficiaries treating more than 1,00,000 OP cases, > 2,25,000 lab investigations, > 8000 X-rays, > 160 surgical procedures etc. The outsourced dialysis ward at DAE Hospital has been continuously utilized by the patients and well appreciated as it has reduced the hardships of patients for commuting to Chennai.

The Administration, Accounts and Auxiliary Departments of IGCAR and GSO have continued to provide commendable services guiding and supporting the execution of the programmes.

I take this opportunity to thank the principals, teachers and staff of Kendriya Vidayalayas, Atomic Energy Central Schools within our township for providing holistic education to our wards. The performance of the students in board exams in all the schools has been exemplary.

This year, apart from the other R & D and regular activities at the various groups of IGCAR and GSO, our focus would continue to be on supporting the activities of PFBR towards Main Vessel Sodium Filling and subsequent First Approach to Criticality, hot commissioning of DFRP, continuing to run FBTR at 40 MWt for more than 100 days, Commissioning of Metal Fuel Laboratory and commissioning and dedication of Doppler Weather Radar Facility.

I look forward to your support and co-operation.

[B. Venkatraman]
Director IGCAR & GSO

Editor's Desk

Dear Reader
Greetings

It is my pleasant privilege to forward the latest issue of IGC Newsletter (Volume 135, January 2023, Issue 1). I thank my team for their timely inputs, cooperation, and support in bringing out this issue.

The New Year Message of Dr. B. Venkatraman, Distinguished Scientist, Director, IGCAR, is included in this issue.

The technical article of this issue "First-Principles Study of Thermodynamic Properties of U with Point-Defects and of U-Pu and U-Zr Alloys" is by Dr. Ravi from MSG, IGCAR.

Young Officer's Forum features an article on "Synthesis of CVD Pyrolytic Graphite at Different Pyrolysis Temperature for Pyrochemical Reprocessing Application" by Shri E. Vetrivendan from MMG, IGCAR.

The article on "Resolving Isobaric interference and accurate measurement of Cs and Sr in the dissolver solution by using Isotopic Dilution Thermal Ionisation Mass Spectrometry (ID-TIMS)" by Ms. Namitha Janardhanan from MC&MFCG, IGCAR is categorised as this issue's Young Researcher article.

In the back cover, we have Jacobin Cuckoo. It is a migrant and arrives in our campus every November.

The Editorial Committee would like to thank all the contributors. We look forward to receiving constructive suggestions from readers towards improving the IGC Newsletter content.

We express our deepest gratitude to Director IGCAR for his keen interest and guidance.

With best wishes and regards

S. Rajeswari
Chairman, Editorial Committee, IGC Newsletter and
Head, Scientific Information Resource Division, IGCAR

First-Principles Study of Thermodynamic Properties of U with Point-Defects and of U-Pu and U-Zr Alloys

Metallic nuclear fuels offer advantages such as higher fissile atom density, higher thermal conductivity that increases with temperature, ease of fabrication and compatibility with coolant. The issues of metallic fuels are associated with its solidus temperature, dimensional stability under irradiation, swelling and fission gas release, and chemical compatibility with cladding. Alloying of U or U-Pu metallic fuels with Zr fixes these issues. Optimal use of these alloys requires that their thermodynamic properties are studied thoroughly. Atomic defects reduce thermal conductivity of nuclear fuel and they govern diffusion hence formation of voids and interstitial loops which deteriorate mechanical performance. The equilibrium concentration of point-defects is governed by their formation energies besides temperature ($c \propto e^{-E^f/k_BT}$). The binding energies of point-defects determine diffusion kinetics ($D \propto c_v e^{-E^b/k_BT}$). Therefore, Density Functional Theory (DFT) calculations of point-defect energies are very common.

Although conventional DFT is often good enough to obtain sufficiently accurate results of point-defect energies in crystals that are stable at ambient temperatures, meaningful results cannot be expected for crystals that are unstable at ambient temperatures but stable at high-temperatures. Figure 1 illustrates this issue. It shows atomic relaxations in supercell models of body centred cubic (bcc) Zr, W and U with a vacancy (denoted by □) obtained from conventional DFT calculations. Structural relaxations show that the atomic displacements are appreciable in Zr and U whereas negligible in W. No atomic relaxations have been observed in pure Zr_{128}, W_{128} and U_{128} therefore not shown. The equilibrium volume and bulk modulus are the most basic physical properties considered when assessing the performance of ab initio approaches. Note that the bcc structure is the ground state of W whereas it is a

high-temperature structure for Zr (1140 to 2128 K) and U (1050 to 1408 K). It is evident from Table 1 that the equilibrium volumes $V(W_{127}\square_1)<V(W_{128})$ whereas $V(Zr_{127}\square_1)>V(Zr_{128})$ and $V(U_{127}\square_1)>V(U_{128})$. This means that vacancy causes expansion of Zr and U lattices whereas contraction of W lattice. This means that the conventional DFT calculation gives undesirable

Table 1. Thermodynamic properties of bcc Zr, W and U obtained from conventional DFT calculations performed with 4×4×4 supercell models with 128 lattice sites

System	Zr_{128}	$Zr_{127}\square_1$	W_{128}	$W_{127}\square_1$	U_{128}	$U_{127}\square_1$
$V(\text{Å}^3)$	2923	2928	2076	2070	2574	2598
$E^f_v(eV)$		-0.86		+3.20		-4.20

volumes and atomic positions for bcc Zr and U with point-defects. Now turn to vacancy formation energies. These energies indicate that W is stable whereas bcc Zr and U are unstable. This means that conventional DFT cannot give desirable point-defect energies of high-temperature phases.

But computation of thermodynamic properties of high-temperature phase of uranium, namely bcc uranium (γ-uranium), is important because the bcc solid solution is the main high-temperature phase of U-Pu-Zr alloy fuel besides α-U, δ-UZr$_2$ and ζ-U$_{0.4}$Pu$_{0.6}$ at ambient temperatures. Moreover, first-principles prediction of thermodynamic properties of high-temperature phases of solids is a challenge in materials physics. First-principles molecular dynamics (FPMD) method offers a robust framework for modelling thermodynamic properties of solids including high-temperature phases. This article reports our study of thermodynamic properties of bcc uranium with point-defects using first-principles molecular dynamics simulations.
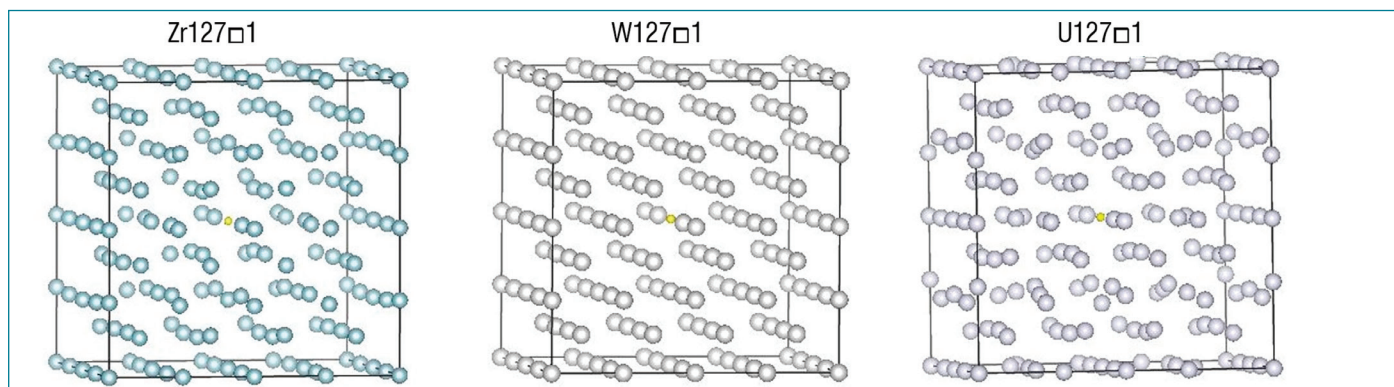

Figure 1: Atomic relaxation in 4×4×4 supercell models of bcc Zr, W and U with a vacancy obtained from conventional DFT calculations (VASP-PAW-PBE-500 eV cutoff-5×5×5 k mesh) with complete relaxation of all structural degrees of freedom. The small sphere at the centre of the super cell indicates the location of a vacancy.

Calculations of formation enthalpy of U-Pu and U-Zr alloys are also discussed briefly.

The formation energy E^f of an atomic defect is a measure of the energy required for its formation. The binding energy of a pair of atomic defects is related to the strength of the attractive or repulsive interaction between them. The equation for E^f of a substitutional defect M, which is either free atoms or pure elements here, is given by: $E^f = E(U_{N-1}M_1) - \frac{N-1}{N}E(U_N) - \frac{1}{n}E(M_n)$ where E ($U_{N-1}M_1$) is the total energy of bcc U supercell with N lattice sites containing (N-1) U atoms and a defect M. E (U_N) is the total energy of pure bcc U supercell with N lattice sites. E (M_n) is the total energy of defect M. For free atom solutes, n is 1 and it is the number of atoms in the unit cell for crystalline solutes. E (M_n) is 0 for M a vacancy. Similar definitions have been used for interstitial formation and vacancy-solute (□-M) binding energies. Point-defects were introduced by removing and/or adding select atoms in the supercell model of the crystal.

The molecular dynamics simulations were performed with ensembles of U_{128}, $U_{127}M_1$, and $U_{126}M_1\square_1$ with substitutional defects M=□, He, Ne, Ar, Kr, Xe, Sr, Zr, I, Cs, and Pu and ensembles of $U_{128}U_1$, $U_{128}He_1$, $U_{128}Kr_1$, and $U_{128}Xe_1$ with self and solute interstitials, disposed on a bcc lattice lying within a 4×4×4 supercell. These solute elements were chosen because they are either fission or decay products or alloying additions in nuclear fuels. The simulations were performed with canonical (NVT) ensembles with temperature controlled using an Andersen thermostat. This thermostat couples the system to a heat bath by stochastic impulsive forces that act occasionally on randomly selected particles. After stochastic collisions, the chosen particle forgets its old velocity and picks its new velocity from a Maxwell-Boltzmann distribution at the imposed temperature. Vienna Ab initio Simulation Package was used to carry out the molecular dynamics simulations with default plane wave basis set cut off and Γ k-point sampling of the Brillouin zone. For the electron-ion interaction, the projector augmented wave (PAW) potentials were used with the Perdew-Burke-Ernzerhof (PBE) generalized gradient approximation for exchange correlation interactions.

Each simulation was performed for 16 ps in steps of 2 fs with temperature T=1100 K. For each system, the MD simulations were performed at three different volumes. The total pressures P and average energies of each of the systems at the three volumes were then fitted to obtain the equilibrium volume (V) and the corresponding energy E at the given T and P. These energies and volumes were then used in the calculations of point-defect energies as well as bulk modulus (B) and volume thermal expansion coefficients (α).

The MD simulations were performed first for bcc Zr and W to establish our computational scheme because FPMD simulations

of uranium with point-defects are scarce. The MD simulations have been used here to calculate the thermodynamic properties of metals with point-defects. Therefore, it is imperative to ensure that the systems retain their structure during the simulation so that the computed properties can be identified with the given phase of the metal. The position auto correlation (PAC) becoming 0 and the mean square displacement (MSD) becoming constant with time are used to assert that the system remain in the same solid state structure during the simulation. The PAC for a chosen atom, i, in a crystal is given by $p_i(t) = \langle(r_i(t+t_0) - R_i^0)(r_i(t_0) - R_i^0)\rangle$ where r_i is the time-varying position of the atom i and R_i^0 is the position of the lattice site of atom i in the perfect crystal structure. The angle brackets denote thermal average which in practice is evaluated as an average over time origins, t_0, and atoms i. For long times t, vibrational displacements become uncorrelated, so that $p_i(t) = \langle(r_i(t+t_0) - R_i^0)\rangle\langle(r_i(t_0) - R_i^0)\rangle \rightarrow \langle r_i - R_i^0\rangle^2$, and if all atoms vibrate about their lattice sites, $\langle r_i - R_i^0\rangle = 0$, so that $p_i(t) \rightarrow 0$ as $t \rightarrow \infty$. The mean square displacement is defined by $\Delta r^2(t) = \frac{1}{N}\sum_i[r_i(t) - r_i(0)]^2$. It is the mean squared distance over which the labelled atoms have moved in a time interval t. The MSD is used here mainly to distinguish between non-diffusive and diffusive behaviour as we are using a thermostat.

Figure 2 shows the average PAC and MSD in Zr_{128}, $Zr_{127}\square_1$, W_{128}, and $W_{127}\square_1$ respectively. It is evident that the PAC and MSD of pure Zr and W and of Zr and W with a vacancy become respectively 0 and constant with time establishing that they remain in the same structure during the simulation (like textbook examples). Though the PAC and MSD of $Zr_{127}\square_1$ approach respectively 0 and constant at a lower rate than those of other systems they essentially indicate that $Zr_{127}\square_1$ also retains its structure during the simulations.

The equilibrium energies of each of these systems at the given temperature T were then obtained from their average energies at the three different volumes through fitting. In all these MD simulations, thermalizations have been reached within about 650 fs. These initial portions of the simulations were omitted when the average energies of the systems were calculated. That is, for every system, a set of three energies, E1, E2, E3, with respective volumes, V1, V2, V3, and pressures, P1, P3, P3 have been obtained. The equilibrium volume of the system, V, corresponding to P=0, is then calculated by fitting the V (P) data to a linear polynomial. The equilibrium energy of the system at P=0 is then calculated by fitting E (V) data to a quadratic polynomial with equilibrium volume V from V (P) fitting. These energies were used in the calculations of formation and binding energies of atomic defects. The bulk modulus, B, and volume thermal expansion coefficient, α, were also calculated respectively from $B = -V\frac{dP}{dV}$ and $\alpha = \frac{1}{BT}\left[\frac{dE}{dV} + P\right]$ at P=0, which are part of the above V (P)
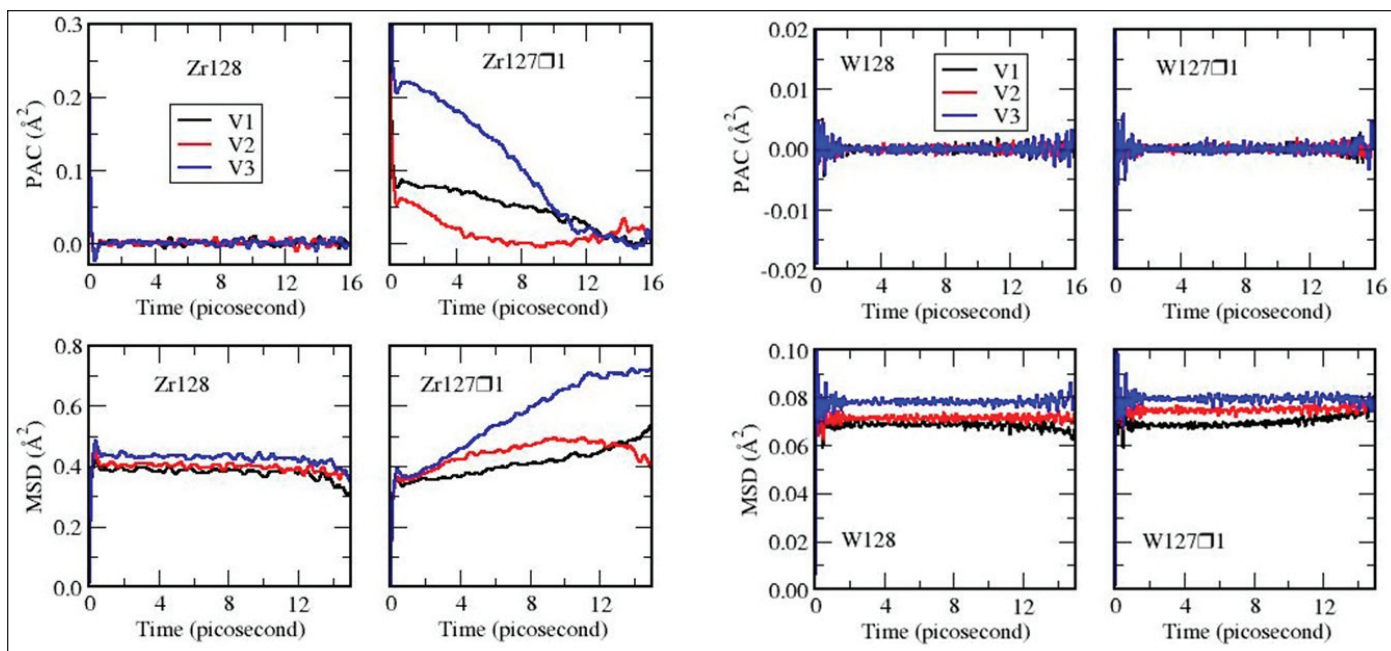
Figure 2. Average position autocorrelation (PAC) and mean square displacements (MSD) in bcc Zr_{128}, $Zr_{127}\square 1$, W_{128} and $W_{127}\square 1$. MD simulations were performed at 1400 K and 1800 K for Zr and W systems respectively at three different volumes V1, V2, and V3 (V1<V2<V3).

and E (V) fitting schemes.

The results of simulations for Zr and W are listed in Table 2. The lattice parameter of pure bcc Zr (3.65 Å) derived from its equilibrium volume at 1400 K is in very good agreement with experimental value (3.627 Å) at 974 K. Our calculated bulk modulus 83 GPa is also in good agreement with the 87 GPa from literature obtained from elastic constants derived from

Table 2. Properties of bcc Zr_{128}, $Zr_{127}\square 1$, W_{128}, and $W_{127}\square 1$ obtained from ab initio MD simulation. The equilibrium volumes (P=0) of simulation supercells, V, together with the vacancy formation energy, E^f_v, are given. Estimates of the bulk modulus, B, and volume thermal expansion coefficients, α, of these systems are also listed

System	V(Å^3)	B(GPa)	$\alpha(10^{-5}/K)$	E^f_v(eV)
Zr_{128}	3048	83	3.02	
$Zr_{127}\square 1$	3031	82	3.31	1.04
W_{128}	2116	294	1.42	
$W_{127}\square 1$	2110	291	1.48	2.90

phonon dispersion curves obtained from inelastic neutron scattering measurements at 1482 K. Our thermal expansion coefficient α of 3.02×10^{-5}/K is also in good agreement with the experimental result 2.96×10^{-5}/K. The vacancy formation energy 1.04 eV deviates from 1.75 eV from literature estimated from specific heat measurements. But the later result is considered to be higher than normal because it leads to a vacancy concentration which is a factor of 10 larger than those obtained with the aid

of the differential dilatometry measurements. Furthermore, the vacancy formation energy is not independent of temperature.

For pure W, our lattice constant of 3.2 Å derived from its equilibrium volume at 1800 K is in very good agreement with the literature value of 3.18 Å. The bulk modulus 294 GPa also is in very good agreement with literature (304 GPa). For the vacancy formation energy, our simulation gives 2.90 eV which is in reasonable agreement with literature (3.1 eV). The differences are likely because our results are for 1800 K whereas literature corresponds to 0 K. The thermal expansion coefficient of W predicted by our work is in good agreement with the literature. These results thus lend credibility to our computational scheme.

We now turn to our results for bcc U with point-defects. The PAC and MSD of U_{128}, $U_{127}\square 1$, and $U_{127}M_1$ with substitutional defects M=He, Ne, Ar, Kr, Xe, Sr, Zr, I, Cs, Pu as well as of systems with self and solute interstitials, namely, $U_{128}U_1$, $U_{128}He_1$, $U_{128}Kr_1$, and $U_{128}Xe_1$ have all been computed and analyzed. Figure 3 shows the PAC and MSD of select systems of U with point-defects. These graphs show that the PAC decrease to 0 and MSD become constant with time. All these systems thus remain in the same structure of uranium during the simulations.

The thermodynamic properties of bcc uranium with point-defects were then calculated in the same manner as described for Zr and W and the results are listed in Table 3. The lattice constant of bcc uranium, 3.50 Å, derived from equilibrium volume V of pure bcc U sueprcell with 128 atoms, 2731.4 Å^3, is in very good agreement with experiment (3.52 Å at 1078 K). Further, the volume V of $U_{127}\square 1$ is reduced relative to pure U_{128}. This
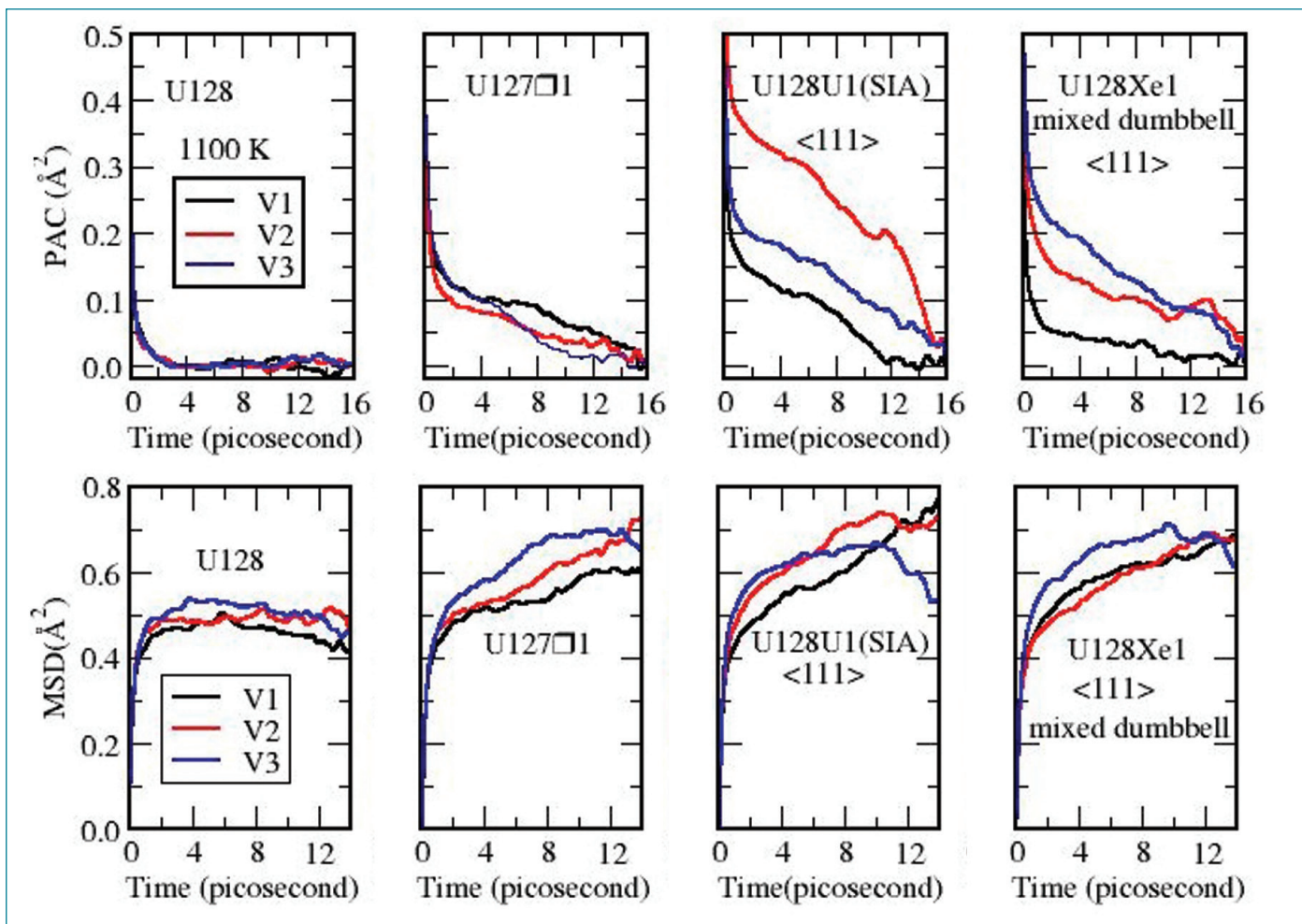
Figure 3. Average position autocorrelations (PAC) (top) and mean square displacements (MSD) (bottom) in bcc uranium at 1100 K without and with point-defects.

is remarkable because conventional DFT predicts volume V of $U_{127}\square_1$ which is higher than that of pure U_{128} by about 1% (Table 1). This is an important improvement by FPMD simulation over the conventional DFT calculation because accurate calculation of equilibrium volume is basic for the reliability of the technique for the other properties computed (Verified that the improvement is not an artefact but natural). Table 3 further shows that the vacancy formation energy E^f_v of bcc uranium is 0.88 eV. Experiments using positron annihilation spectroscopy have determined this energy to be 1 eV and 0.3 eV which are quite different. Moreover, our

Table 3. Thermodynamic properties of bcc U with point-defects obtained using FPMD simulations at 1100 K. The equilibrium volumes of supercells, V, together with formation energies, E^f, of atomic defects are given. Estimates of bulk modulus, B, and volume thermal expansion coefficients α are also listed. The last four rows on the right side are data for self and solute interstitials in their respective low energy dumbbell configurations.

System	V(Å^3)	B(GPa)	$\alpha(10^{-5}/\text{K})$	E^f(eV)	System	V(Å^3)	B(GPa)	$\alpha(10^{-5}/\text{K})$	E^f(eV)
U128	2731.4	109	2.21		$U_{127}Zr_1$	2738.1	104	3.22	0.92
$U_{127}\square_1$	2715.7	102	3.24	0.88	$U_{127}I_1$	2745.4	101	4.12	2.02
$U_{127}He_1$	2731.0	103	3.44	1.70	$U_{127}Cs_1$	2755.2	98	3.33	5.24
$U_{127}Ne_1$	2735.8	101	3.56	2.54	$U_{127}Pu_1$	2730.8	102	4.34	0.25
$U_{127}Ar_1$	2740.4	101	3.94	5.38	$U_{128}U_1$	2758.0	109	4.31	1.06
$U_{127}Kr_1$	2747.3	101	3.14	5.58	$U_{128}He_1$	2751.0	107	3.24	1.76
$U_{127}Xe_1$	2753.2	102	3.72	6.46	$U_{128}Kr_1$	2768.0	111	2.32	6.28
$U_{127}Sr_1$	2753.1	97	4.76	2.10	$U_{128}Xe_1$	2772.8	113	2.48	6.52

E^f_v of α-U, 1.84 eV from conventional DFT is in good agreement with 1.6±0.2 eV from literature. In view of these, our 0.88 eV for E^f_v of bcc U is more reliable. For the formation energies of other solute atom defects neither experimental nor FPMD-based results available in the literature.

The formation energies of noble gas atoms show that they bear a relation to their size. This apparent size effect on point-defect formation energies is not evident for other solutes, namely, Sr, Zr, I, Cs and Pu. Since these solutes are chemically reactive, their formation energies appear to be influenced by both size and chemical effects.

Figure 4 presents the schematics of high symmetry interstitial dumbbell configurations in bcc lattice on the left and self and solute interstitial formation energies on the right panels. It is evident that the self interstitial formation energies are lower than those of solute interstitials. That is, bcc U accommodates self interstitials more easily than decay or fission gas interstitials (He, Kr, Xe). The minimum self interstitial formation energy 1.06 eV is higher than the vacancy formation energy 0.88 eV. This indicates that vacancies are favourable point-defects in bcc uranium. We can also see from figure 4 that interstitial Xe has lowest formation energy 6.52 eV in <111> dumbbell configuration against substitutional formation energy 6.46 eV (Table 3). Note also that the atomic volumes of Xe in these configurations are not comparable.

The bulk modulus 109 GPa for pure bcc U (Table 3) is in good agreement with experiment (113 GPa) from literature. Bulk moduli of bcc U with point-defects tend to be reduced relative to that of pure bcc U. The bulk moduli of bcc U with self and solute

interstitials are of the same order as with substitutional solutes. It is difficult to distinguish between substitutional and interstitial solutes from their effect on bulk modulus of the host crystal.

The volume thermal expansion coefficient α of pure bcc U (Table 3) obtained using FPMD simulation (2.21×10^{-5}/K) is in agreement with experiment (2.46×10^{-5}/K) from literature. This allows that our thermal expansion coefficients of other systems are useful estimates. The thermal expansion coefficients of bcc U with point-defects are generally increased substantially relative to that of pure bcc U. Note that our model corresponds to point-defect concentrations less than 1.6%. Thermal expansion coefficient of bcc U with this defect concentration is not generally found in the literature. Dilatometry curves of U-Zr alloys from literature show that Zr causes α to increase relative to pure U which appears to agree with the increased thermal expansion coefficient of $U_{127}Zr_1$ from our work.

The binding energies of solutes to vacancy determine their diffusion kinetics. Table 4 lists the $\square$-M binding energies E^b together with equilibrium volumes V of the supercells. Estimates of bulk modulus B and thermal expansion coefficient α of bcc uranium with pair point-defects are also listed. We see that the equilibrium volumes of $U_{126}M_1\square_1$ are reduced relative to respective equilibrium volumes of $U_{127}M_1$ for all M (Table 3). The reductions in volume vary from 14 to 19 Å^3 which are comparable to the atomic volume of U (20.84Å^3). The bulk modulus of $U_{126}M_1\square_1$ tends to be reduced relative to those of respective $U_{127}M_1$. For instance, B of $U_{127}\square_1$, $U_{127}He_1$, and $U_{126}He_1\square_1$ are respectively, 102, 103 and 99 GPa. That is, B of $U_{126}He_1\square_1$ is lower than those of $U_{127}\square_1$ and $U_{127}He_1$. This appears to be reasonable. But
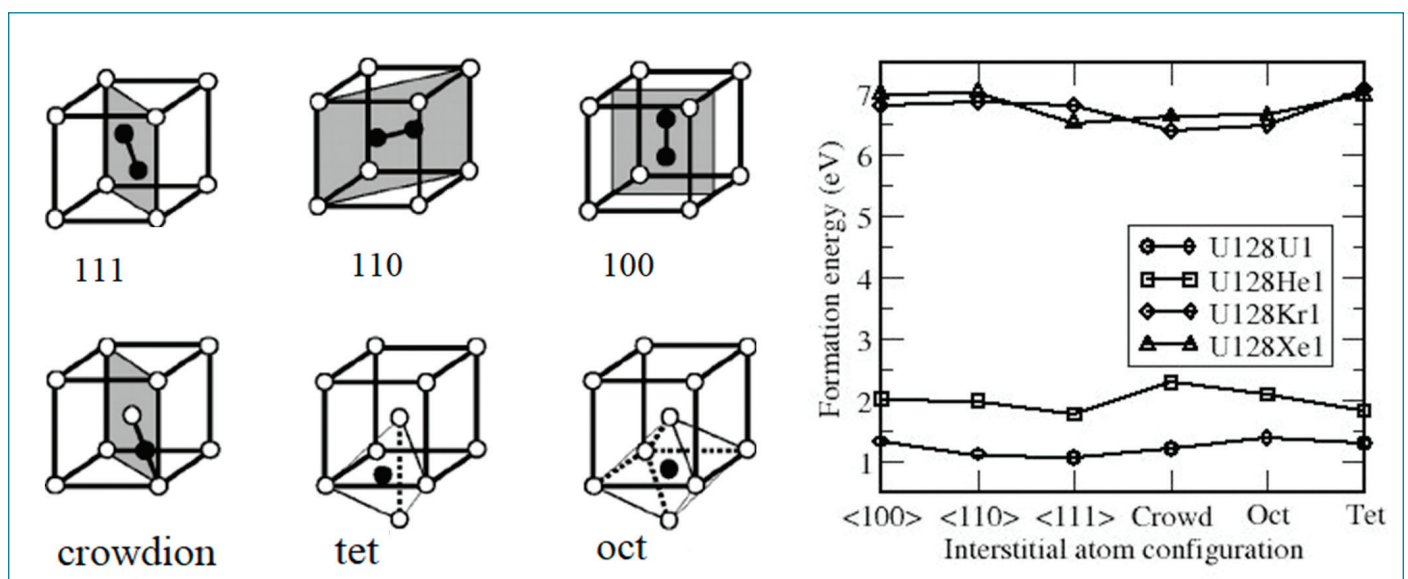

Figure 4. High symmetry interstitial dumbbell configurations in bcc crystal (left): Self and solute interstitial formation energies in bcc uranium with respect to interstitial configuration (right). The x-axis labels <100>, <110>, <111>, Crowd, Oct and Tet correspond respectively to split dumbbells, crowdion, octahedral, and tetrahedral interstitial configurations.

Table 4. Properties of $U_{126}M_1\square_1$ obtained with the aid of FPMD simulations at 1100 K. The binding energies E^b of atomic defects in bcc uranium and their equilibrium volumes V are listed. Estimates of bulk modulus B and thermal expansion coefficient α are also listed.

System	V($Å^3$)	B(GPa)	$\alpha(10^{-5}/K)$	E^b(eV)
$U_{126}\square_1\square_1$	2702.2	104	3.64	+0.31
$U_{126}He_1\square_1$	2713.6	99	4.20	-0.37
$U_{126}Ne_1\square_1$	2719.6	97	3.81	-0.22
$U_{126}Ar_1\square_1$	2721.9	100	4.12	-0.18
$U_{126}Kr_1\square_1$	2730.0	104	2.90	-0.36
$U_{126}Xe_1\square_1$	2735.1	103	1.84	-0.68
$U_{126}Sr_1\square_1$	2738.2	93	4.75	-0.52
$U_{126}Zr_1\square_1$	2719.8	103	3.82	-0.23
$U_{126}I_1\square_1$	2729.0	103	2.66	-0.84
$U_{126}Cs_1\square_1$	2739.0	102	2.64	-0.64
$U_{126}Pu_1\square_1$	2712.2	100	4.68	-0.46

Table 5. Formation enthalpy ΔH^f of orthorhombic and bcc U-Pu and U-Zr alloys from conventional DFT calculations. Special quasirandom structures were used to model the alloys.

U-Pu alloys	ΔH^f (eV/atom)	U-Zr alloys	ΔH^f(eV/atom)
Orthorhombic		Orthorhombic	
$U_{99}Pu_9$	0.01	$U_{99}Zr9$	0.08
$U_{90}Pu_{18}$	0.01	$U_{90}Zr18$	0.14
$U_{81}Pu_{27}$	0.01	$U_{81}Zr_{27}$	0.13
$U_{54}Pu_{54}$		$U_{54}Zr_{54}$	0.14
Cubic		Cubic	
$U_{120}Pu_8$	-0.28	$U_{120}Zr_8$	-0.21
$U_{112}Pu_{16}$	-0.38	$U_{112}Zr_{16}$	-0.16
$U_{104}Pu_{24}$	-0.44	$U_{104}Zr_{24}$	-0.14
$U_{96}Pu_{32}$	-0.54	$U_{96}Zr_{32}$	-0.12
$U_{88}Pu_{40}$	-0.60	$U_{88}Zr_{40}$	-0.11
$U_{80}Pu_{48}$	-0.68	$U_{80}Zr_{48}$	-0.10
$U_{72}Pu_{56}$	-0.74	$U_{72}Zr_{56}$	-0.08
$U_{64}Pu_{64}$	-0.82	$U_{64}Zr_{64}$	-0.07

there are exceptions. Quantitative comparison would require more accurate simulations with better system size and k-point sampling. Our divacancy binding energy of 0.31 eV in bcc U is similar to 0.30 eV in bcc Fe. Comparison of our solute-vacancy and divacancy binding energies suggest that nucleation and growth of fission gas bubbles are supported by a thermodynamic driving force which is absent for void formation from vacancies joining together.

As stated earlier, optimal use of metallic alloy fuel requires that their thermodynamic properties studied thoroughly. Formation enthalpy is a key quantity encapsulating phase stability. Orthorhombic and bcc phases are predominant phases in U-Pu-Zr alloys. Therefore, formation enthalpies of orthorhombic and bcc phases of U-Pu and U-Zr alloys were computed using special quasirandom structures (SQS). SQS represents the best periodic supercell approximation to the true disordered state for a given number of atoms per supercell. For the orthorhombic alloy, four SQS namely, $U_{99}Pu_9$, $U_{90}Pu_{18}$, $U_{81}Pu_{27}$ and $U_{54}Pu_{54}$ were generated based on 3×3×3 supercell of orthorhombic α-uranium. For bcc alloy, eight SQS, namely, $U_{120}Pu_8$, $U_{112}Pu_{16}$, $U_{104}Pu_{24}$, $U_{96}Pu_{32}$, $U_{88}Pu_{40}$, $U_{80}Pu_{48}$, $U_{72}Pu_{56}$, and $U_{64}Pu_{64}$ were generated based on 4×4×4 supercell of bcc uranium. Pu is replaced with Zr to get U-Zr SQS. The SQS were generated using the alloy theoretic automated toolkit (ATAT). Table 5 lists our

conventional DFT computed formation enthalpies of these alloys. These formation enthalpies show that the bcc alloys are stable with respect to bcc U and Pu in agreement with their phase diagrams whereas the orthorhombic alloys are unstable with respect to orthorhombic U and monoclinic Pu. Orthorhombic alloys are unstable likely because our alloy concentrations are beyond their solubility limits. No literature corresponding to our results on formation enthalpies of U-Pu and U-Zr alloys are available for comparison.

In conclusion, thermodynamic properties of bcc uranium (a high-temperature phase) with point-defects have been studied successfully using ab initio molecular dynamics simulations with canonical ensembles of $U_{127}M_1$, $U_{128}M_1$, and $U_{126}M_1\square_1$ for M=$\square$, He, Ne, Ar, Kr, Xe, Sr, Zr, I, Cs, and Pu. This work provides formation energies of substitutional, self and solute interstitial defects as well as binding energies of $\square$-M pair defects besides estimates of bulk modulus and volume thermal expansion coefficients. Binding energies of divacancy and solute-vacancy pairs indicate that nucleation and growth of fission gas bubbles are supported by a thermodynamic driving force over void formation (see Ravi et al, Physical Review Materials 5, 053604 (2021)). Using special quasi random structures, phase stability of U-Pu and U-Zr alloys have been examined through their computed formation enthalpies.

Young Officer's Forum

Mr. E. Vetrivendan is working as a Scientific Officer 'E' at the Corrosion Science and Technology Division, Indira Gandhi Centre for Atomic Research. He acquired his B.Tech. (Metallurgy) and M.E (Materials Engineering) degrees from NIT Trichy and IISc, Bangalore. Recipient of the DAE Young Engineer Award 2019 and currently pursuing PHD in HBNI. His research interests include the development, testing and characterization of thermal spray and CVD coatings for reactor and reprocessing applications. He has authored/co-authored 25 peer-reviewed research articles in international journal

Synthesis of CVD Pyrolytic Graphite at Different Pyrolysis Temperature for Pyrochemical Reprocessing Application

Nuclear grade graphite and pyrolytic graphite (PyG) are proposed construction materials for high-temperature molten LiCl-KCl for the pyrochemical reprocessing of metallic fuel and also as structural/core materials for molten salt reactors (GEN IV reactor). Pyrolytic graphite (PyG) is synthetic polycrystalline graphite produced by the thermal pyrolysis of hydrocarbons by chemical vapour deposition (CVD) at very high-temperatures. In the vapour deposition technique, since the material build-up on the hot surface is essentially atom by atom with an orientation of graphitic planes parallel to the substrate surface, PyG exhibits a high degree of preferred orientation and anisotropy. In PyG, no orderly relation exists in the stacking of layer planes, which destroys the periodic repetition of lattice positions in the thickness direction resulting in a turbostratic arrangement with an interlayer distance of about 3.44 Å. PyG is an ultra-high pure carbon with near theoretical density with zero porosity, resulting in extreme chemical inertness and stability at high-temperatures. Because of the layered arrangement, PyG shows a marked degree of anisotropy in physical, thermal, and electrical properties. Traditional moulded/extruded commercial graphite consists of carbonaceous raw material with additives like resins and binders, baked and graphitized to enhance specific properties, while PyG is chemically pure crystalline carbon deposited from vapour with no binders or other impurities. Thus, PyG exhibits superior chemical and mechanical properties compared to its conventional graphite counterparts.

The properties of CVD-grown PyG coatings on high density graphite (HDG) substrates are strongly dependent on the microstructure, density, degree of orientation, and the graphitization and defects concentration. The nucleation and growth modes of PyG in a CVD process are mainly determined by vis., the physical condition of the substrate, gas dynamics at substrate surface (flow rate, pressure, velocity, boundary layer thickness, resident time, etc.), and pyrolysis temperature. The influence of pressure and pyrolysis temperature on the microstructure and density of PyG are distinct. Specifically, the pyrolysis temperature effects significantly alter the diffusion coefficients of species, boundary layer thickness, pyrolysis reaction, and growth kinetics over pressure effects. The texture, crystallinity, and growth rate kinetics for PyG produced under the full spectrum of pyrolysis starting from 1400 °C going up to a maximum of 2400 °C are investigated.

Experimental - CVD deposition of Pyrolytic Graphite:

Commercially available fine-grained HDG of density $\sim$1.86 g/cm^3 of dimensions $5\times10\times50$ mm was used as the substrates to synthesize PyG coatings. Substrate surfaces were prepared with 600 mesh emery sheets with edges smoothened off and cleaned by ultrasonication in ethanol to remove surface contaminants. HDG substrates were made hanging using tungsten wire from a perforated graphite fixture seated inside the hot zone. In the present investigation, PyG coatings were synthesized at different pyrolysis temperatures, i.e., 1400, 1600 °C for 2 h to have a good thickness build-up for ease of characterization and 1700 to 2400 °C for 1 h deposition time, maintaining isobaric ($\sim$2.5 mbar) condition with constant flow rates of gases. Density measurements were carried out using the delaminated, PyG films using a sink-floatation method in a miscible solution of bromoform (2.89 g/cm^3) with

ethanol (0.78 g/cm3). The interplanar distance, anisotropy, and the degree of crystal orientation of PyG grown at different pyrolysis temperatures were studied using XRD. The structural bonding fingerprints and in-plane and out-of-plane defects concentration in the PyG coatings are investigated using Laser Raman Spectroscopy (LRS). The phase purity and degree of sp2 hybridization in PyG coatings were analyzed by x-ray photoelectron spectroscopy (XPS) using an excitation source of monochromatic Al Kα (1486.7 eV) x-ray radiation. The PyG being an optically anisotropic material (birefringent), polarized light optical microscopy (PLM) in cross polarized condition produces cross-section imaging with improved contrast. The analyzer is rotated until a precise minimum intensity is achieved, and the angle of the analyzer at this minimum intensity is called the extinction angle (Ae). Depending on the angle, the textures of the PyG coatings are defined qualitatively as low, medium, and high textures.

Results:

The density of PyG films synthesized at different pyrolysis temperatures by sink and floatation technique are shown in Fig. 1. It is evident that the density of PyG is strongly dependent and has a direct relationship with the temperature reaching a maximum plateau (density >2.2 g/cm3) at 2100 °C and above. Below 1800 °C, there exists a gradual drop-in density to 1.96 g/cm3 at 1400 °C. The density of PyG is a critical parameter that defines all other physical, chemical, thermal, and electrical properties.

In PLM, the intensity of light after the analyzer of optical anisotropic and birefringent materials like PyG is dependent on the optical properties (texture) like the reflection coefficient of ordinary and extraordinary rays (Ro/Re) and their relative phase shift, the orientation of the optical axis (001) for graphite relative to the polarization of incoming light and angle of analyzer. For the investigation of Ae, the coating cross-section is oriented with the preferred orientation of the layers (or the optical axis of PyG) at an angle of 45° relative to the direction of the polarizer or analyzer in cross-polarized condition. The angle of the analyzer for minimum
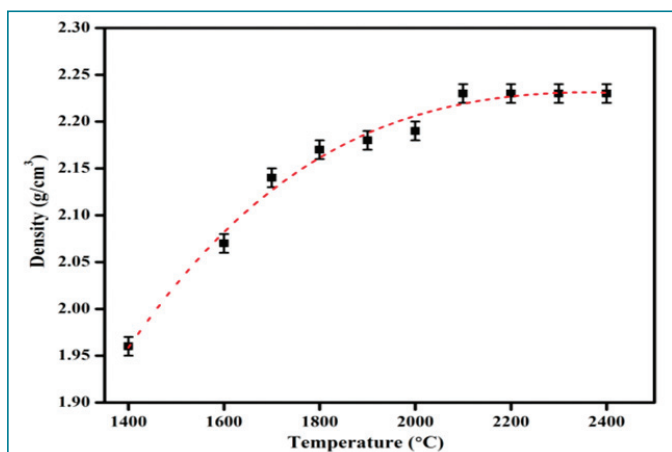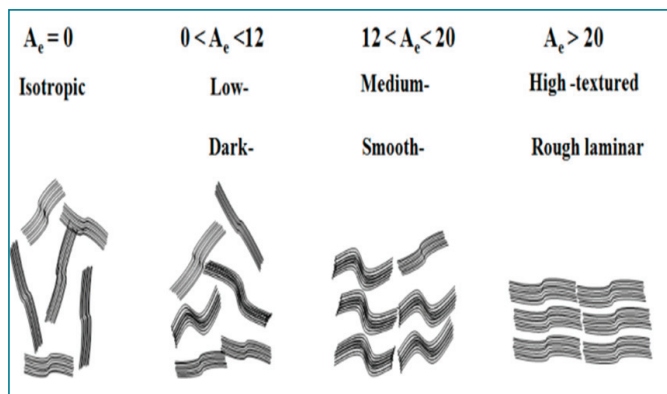

Figure 2: Schematic representation of the varying degree of texture with Ae.

intensity relative to the direction perpendicular to the polarizer is reported as Ae. The value of Ae measured experimentally for the PyG coatings synthesized at pyrolysis temperature from 1400 to 2400 °C are shown in Table 1. It is evident that Ae exhibit the maximum value of 22.5° for PyG at 2400 °C and gradually decrease to 19° at 1600 °C and sudden drop to 7° for 1400 °C synthesized PyG. The Ae decreases monotonously with the decrease in the degree of anisotropy of reflection coefficients. The relationship between the degree of preferred orientation or the texture with the extension angle Ae is represented in Figure 2. Thus, the degree of texture in PyG is strongly dependent on the pyrolysis temperature.

Table 1: Calculated Ae by PLM for PyG synthesized from 1400 °C to 2400 °C.	
Sample	**Extinction angle (°)**
PyG_1400 °C	7.5
PyG_1600 °C	19
PyG_1800 °C	21
PyG_2000 °C	21.5
PyG_2200 °C	22
PyG_2400 °C	22.5

The XRD peaks recorded from the top surface of PyG films synthesized at pyrolysis from 1400 to 2400 ºC under normalized acquisition conditions show a intense, sharp peaks for the (002) basal plane observed across the PyG samples and the absence of isotropic peaks represent the high degree of preferred orientation. The orientation density is given by the integrated intensity of the (002) peak, proportional, and represents a fraction of the peak intensity, varying from sample to sample. In comparing the preferred orientation of different PyG samples, the variation in proportionality between integrated intensity and peak intensity can be compensated by normalizing the measurement, considering $I_{(002)max}$=1. Figure 6 represents the results of qualitative comparison of preferred orientation of different PyG samples,

Figure 1: Plot showing the density of PyG films vs. pyrolysis temperature.

which is a plot of normalized peak and integrated intensity $I_{(002)}$ with respect to maximum intensity, i.e., 2400 °C pyrolysis PyG $I_{(002)}$ =1. The plot summarizes that both normalized peak and integrated intensity values follow a perfect monotonous decreasing trend with decreasing pyrolysis temperature or, in another way, an increase in the degree of preferred orientation with increasing pyrolysis temperature.

The LRS recorded for the PyG synthesized from 1400 to 2400 °C are stacked and shown in Figure 4. The intense sharp and narrow G peak with $FWHM_G$ ranging from 21-28 cm^{-1} represents an overall high degree of graphitization for all the PyG materials. The slight blue shift in the G peak position (>1582 cm^{-1}) indicates the presence of internal compressive strain, and its magnitude is directly proportional to the Raman shift [29, 30]. A low intensity of disorder-induced D peak (between 1336 to 1338 cm^{-1}) and D' peak is evident in the spectrum with the intensity ratio of I_D/I_G much less than unity (<0.2) across PyG samples at different pyrolysis temperatures. The presence of sub-domain boundaries, columnar grown cone boundaries, and planar defects in the PyG structure contributed to the activation of D band peaks. The observance of a broad 2D peak with almost half (~0.6 times) the intensity of G peak and singe Lorentzian profile with $FWHM_{2D}$ line of ~ 33 to 46 cm^{-1} indicate the turbostratic random orientation and corresponding electronic coupling between the graphene layers being absent. Thus, from the structure analysis of different PyG samples, it is evident from the maximum blue shift in G peak position, the highest value of $FWHM_G$, $FWHM_D$, and I_D/I_G is observed for PyG synthesized at 1800 °C; and thereby indicating maximum internal strain, planar defects, and disorders.

The C1s XPS spectra obtained and the peak fit analysis using Gaussian-Lorentz functions for PyG synthesized from 1400 to 2400 °C are shown in Figure 5. It is evident that the C1s peak fit analysis, the predominant bond type, is sp^2 hybridization, i.e., the
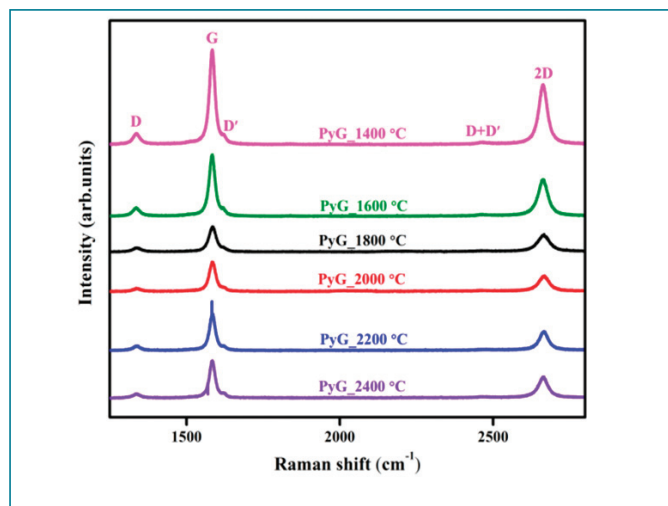

Figure 4: LRS of PyG films synthesized at different pyrolysis temperatures.

complete graphitic arrangement of carbon atoms with contributions (>90%) across PyG samples. Intermediate pyrolysis temperature, i.e., at 1800 °C, showed anomalous behaviour as in the case of LRS too, exhibited maximum presence of sp^3 and C-O bond type contributed to ~8.9%. Going on either side of 1800 °C pyrolysis, the sp^2 content increase gradually to a maximum of ~95% with a corresponding reduction in the defects fractions (sp^3 + C-O). The ratios of sp^2:defects ratio shown a maximum ratio of 23:1 for 2400 °C pyrolysis reveal a high degree of graphitization with lower defects.

The SEM surface topography of the PyG films grown on HDG substrate at different pyrolysis temperatures is shown in Figure 6. Surface micrographs reveal cauliflower morphology typical of columnar grown heads resembling John-Mehl tessellations with triple point boundaries. The average size of the polygonal grains measured on the surface shows a direct correspondence with pyrolysis temperature.

The growth of anisotropic PyG by the low-pressure CVD process on HDG substrate follows a Volmer-Weber 3D island growth model that accounts for the grain size, shape, and formation tessellation surface with triple point grain boundaries. The growth of carbon layers is initiated by heterogeneous nucleation (~10^{10} cm^{-2}s^{-1}) of isolated hemispheres (germs) at active sites on the HDG substrate after a short incubation time. Once a stable nucleus is formed, it grows radially in all directions with a constant velocity until it impinges and coalesces with the adjacent nucleus, extending with different orientations, forming a grain boundary until a continuous film covers the substrate surface. The columnar growth on each nucleus happens by the concentric deposition of new graphitic layers around each nucleus. The growth continues on the dominant nucleus forming parabolic-shaped cones terminating the later seed nucleus growth by forming a boundary between them.
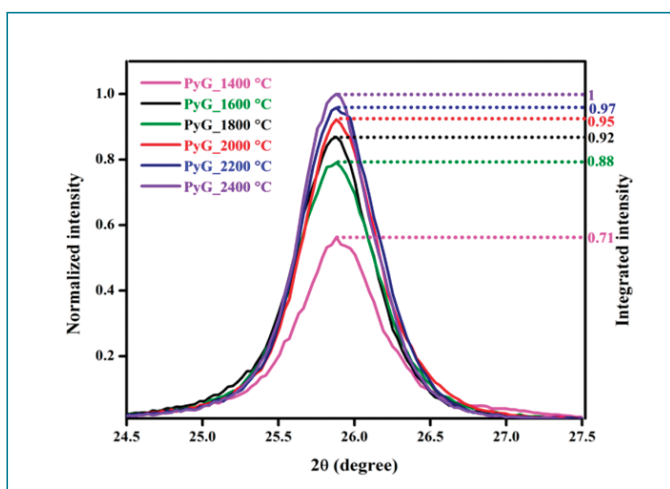

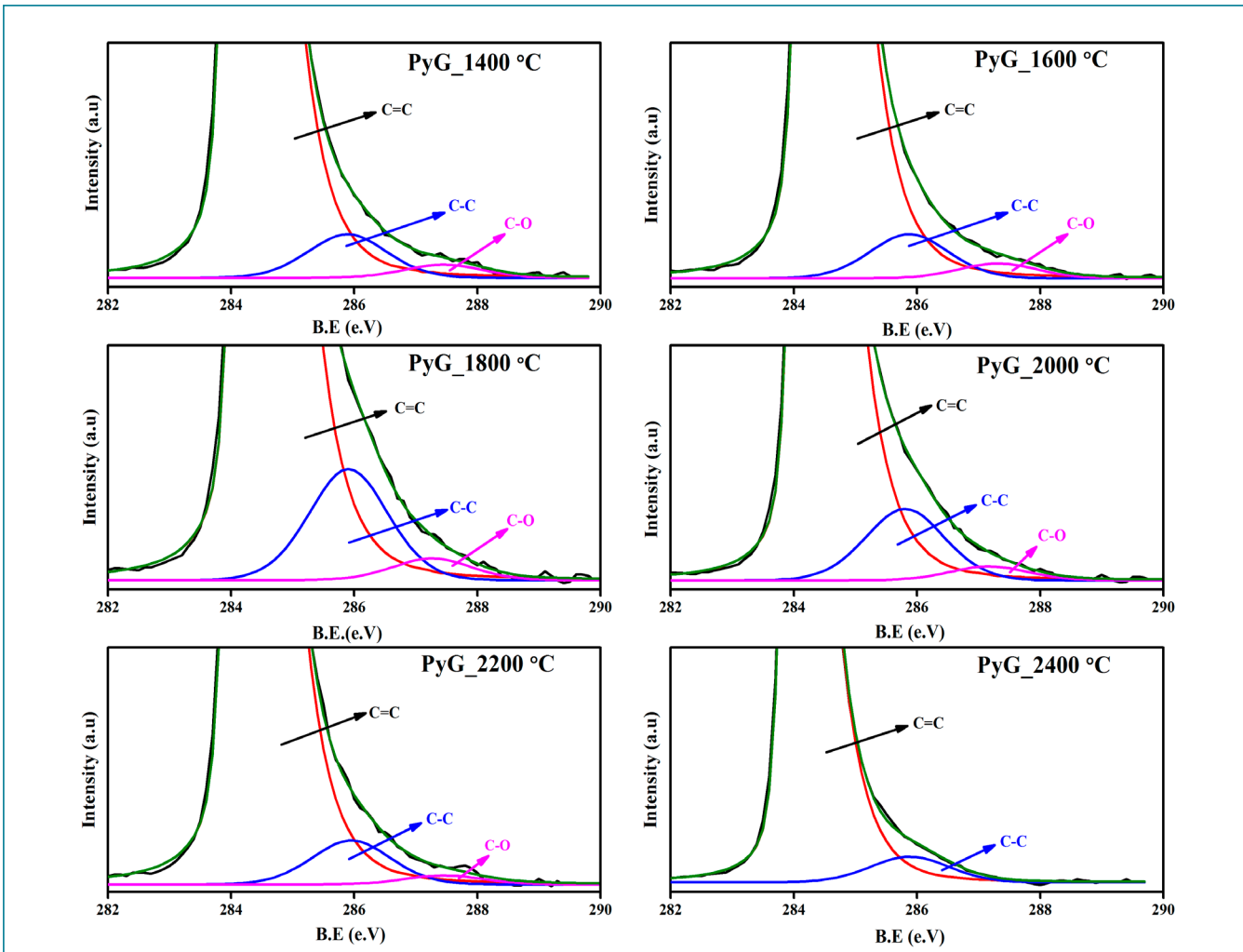Figure 3 : Comparison of the peak, the integrated intensity of (002) peak by normalizing I(002)max.=1.

Figure 5: The peak fit analysis for relative area in C1s XPS spectra of PyG synthesized at different pyrolysis temperatures.

Consequently, the columns or cones based on the nucleus seeded earliest on projected peaks on the substrate surface dominate the structure with time. This explains the decrease in the number

Figure 6: SEM surface morphology PyG synthesized at different pyrolysis temperatures.

of polygonal grains or increase in cauliflower head size on the tessellation surface with PyG film growth.

The increase in PyG pyrolysis temperature show a monotonous increase in density and preferred orientation of graphitic layers as evidenced by extinction angle in PLM, normalization of $I_{(002)}$ in XRD and tortuosity in graphite stacking. Raman spectroscopy analysis for G band position, $FWHM_G$ band, I_D/I_G ratio and sp^2:defects ratio from C1s XPS spectra of PyG synthesized at 1800 °C show more strain and relatively higher defects structures. The 3D island growth model explains the surface nucleation and columnar growth with cone morphology, producing a tessellation surface with polygonal elements. Low temperature PyG pyrolysis <1600 °C results in dark laminar texture with isotropic properties suitable for sealing nuclear graphite to improve chemical resistance for Gen IV reactors and bio-medical implants. While for applications like a rocket nozzle, thermal managements, semiconductors, magnetic levitation etc., anisotropic rough texture produced at pyrolysis >1800 °C is most suitable.
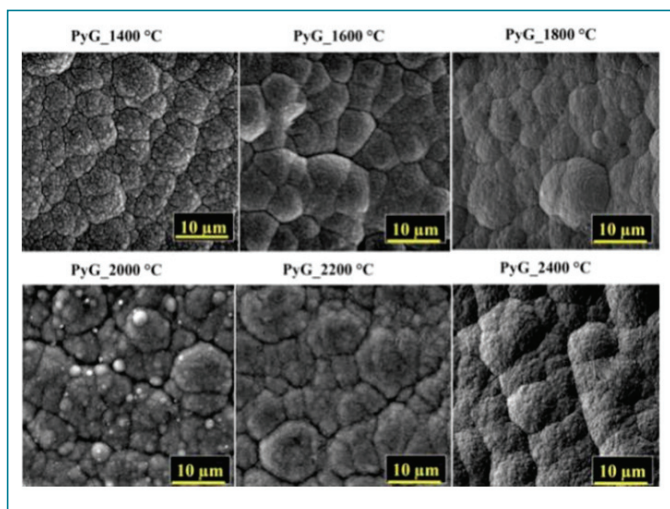
Young Researcher's Forum

Ms. Namitha Janardhanan is pursuing her doctoral degree under HBNI in Analytical Chemistry and Spectroscopy Division, MC&MFCG, IGCAR. She has completed her Bachelors in Chemistry from Govt. Victoria College, Kerala and Awarded for Outstanding Academic Performance. She received her Masters in Chemistry from PSG College of Arts & Science, Coimbatore. Currently, she is working in the area of some novel application of Laser Induced Breakdown Spectroscopy and Mass Spectrometry based analytical instruments towards the analysis of few inorganic systems that are encountered in nuclear fuel cycle. She has published three papers in peer-reviewed international journals so far towards her Ph.D work and attended four conferences and received one Best Poster Award. In addition, she has contributed to works published in five other publications.

Resolving Isobaric interference and accurate measurement of Cs and Sr in the dissolver solution by using Isotopic Dilution Thermal Ionisation Mass Spectrometry (ID-TIMS)

One of the major goals of nuclear programmes involving a closed-fuel-cycle is to have an effective procedure for the management of high active waste (HAW), which is generated during the extraction of U and Pu from a spent fuel. A concentrated form of HAW from a reprocessing plant is known as high level liquid waste (HLLW), containing all the non-volatile fission products (FPs). Among these FPs, determination of radioactive Sr and Cs isotopes is crucial due to the following reasons: (i) the environmental risk, i.e. these isotopes can get into the biological pathway, due to their chemical similarity, namely Sr is similar to Ca and Cs to that of K; (ii) from waste management point of view, i.e. in HLLW, ^{90}Sr and ^{137}Cs are of major concern, as they are relatively long-lived isotopes, emit high energy radiation and have reasonably higher fission yields, resulting in higher radiation heat load in the waste than any other FPs. Much effort has been put into developing various methods to determine these isotopes. Both radiometric and mass spectrometric methods have been reported. Use of radiometric method for the determination needs the separation of these elements in to its pure fraction, as the beta energy spectra is continuum and it is difficult to deconvolute the spectra when other beta emitting FPs are present. Compared to radiometric method, mass spectrometric method for the quantitative determination of long lived radio isotopes is better, because of its high accuracy, easy to analyze and have high sensitivity. But in a mass spectrometric (MS) method, one needs to address the issues related to isobaric interferences. The interference to ^{137}Cs isotope mainly comes from ^{137}Ba, and for ^{87}Sr & ^{90}Sr due to ^{87}Rb & ^{90}Zr, respectively. Hence, in MS method too, there is a need for a chemical separation procedure for the removal of isobaric interfering elements. Such pre-separation procedures are time consuming, tedious and generate additional secondary radioactive waste. Earlier, efforts were done by different groups to mitigate the need for pre-separation procedures by using a reaction/collision cell, when mass analysis is done by using quadrupole (ICP-QMF); or by changing of plasma power, when mass analyser used is magnetic sector (ICP-SFMS). However, with the above kind of ICP-MS analysis, both Cs and Sr cannot be measured in a single run; because the experimental conditions used for the measurement of Cs are very different from that of Sr. To the best of our knowledge, all the reported studies based on ID-TIMS for the quantitative determination of ^{137}Cs and ^{90}Sr (both present in a given sample) have adopted a prior chemical separation to get pure fractions of Cs and Sr prior to the mass analysis. Hence, there is a need to develop a method for the quantitative determination of ^{137}Cs and ^{90}Sr based on TIMS, without pre-separation. Towards this objective, we demonstrate the quantitative determination of ^{90}Sr and ^{137}Cs present in an actual dissolver solution of spent fuels obtained from thermal and fast reactors using TIMS, without chemical separation. To our knowledge, this is first of its kind.
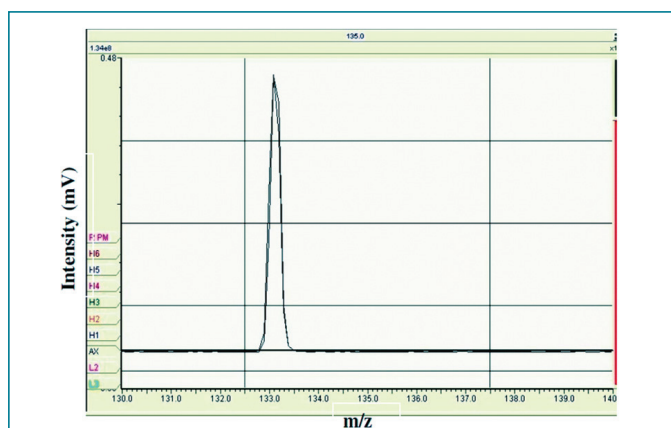
Fig. 1 Mass spectrum of Cs obtained at a filament current of 1.3 A; no interference from Ba is observed.

A thermal ionization mass spectrometer (M/s IsotopX, U.K.) of Isoprob-T model was employed for the isotopic composition and concentration measurements. In order to optimize the experimental conditions for the radioactive samples, initial experiments were carried out with natural abundance, i.e. non-radioactive sample mixture containing Sr, Rb, Cs, Zr and Ba, prepared from spectroscopic grade reference solutions. We have used a mixture of $H_3PO_4 + Ta_2O_5$ as activator and observed good intensities for both Sr and Cs. Preferential evaporation method is adopted for the analysis of elemental species that are present in a mixture, as there are considerable differences exist in some of their thermophysical properties such as enthalpy of vaporization, vapor pressure and ionization energy. During analysis, Cs ions start appearing at 1.1 A of filament current and measurements were carried out at 1.3 A (corresponding filament temperature of 1000 K) to have stable and sufficient ($\sim$600 mV) ion intensity for precise isotopic ratio measurement. As Cs has the lowest enthalpy of vaporization, the lowest ionization energy (IE) and very high vapor pressure, it is expected to get vaporized and ionized first. A typical mass spectrum obtained (for a mass range of 130 to 140 amu, covering all the possible isotopes of Cs and Ba) at a filament current of 1.3 A is shown in Fig. 1. As can be seen, no isotopes of Ba are observed in the mass spectrum, as its enthalpy of vaporization is about 2.5 times higher than that of Cs; the corresponding vapor pressure of Ba is five orders of magnitude lower; furthermore, the IE of Ba (5.21 eV) is much higher than that of Cs (3.89 eV). The signal for Cs is found to be stable ($\sim$600 mV, at a filament current of 1.3 A) and no definite change in intensity was observed even for long time (2–3 h). When the filament current is increased above 2.0 A (1265 K), then the Ba isotopes have started appearing. Thus, it is possible to measure the Cs isotopes without any isobaric interference from the isotopes of Ba.

After Cs analysis, the filament was maintained at high-temperature (2.1 A/1280 K) for up to 3 h to remove the isobaric interference

of Rb in the isotopic ratio (IR) measurement of Sr. At this filament current of 2.1 A, very weak signal of Sr ions ($<$1 mV) appeared, implying that there will be minimum loss of Sr (thus sufficiently available at measuring condition of 2.6 A/1450 K) and quick burning out of Rb from the sample (as there is considerable difference in the enthalpy of vaporization of Sr and Rb; and the value for Rb is very close to that of Cs).

Sr isotopic ratio measurement was carried out at 2.6 A where a sufficient ($\sim$600 mV) ion intensity for Sr isotope (major isotope) was observed. As can be seen from the mass spectrum in Fig. 2, covering a mass range of 83–90 amu, only isotopes of Sr are observed and no isotope of Rb is present; the same is expected, as the enthalpy of vaporization of Sr is 2 times higher than that of Rb and the corresponding vapor pressure of Rb is 150 times higher than that of Sr. Thus, at this filament current of 2.6 A, there is no isobaric interference due to [87]Rb in the determination of [87]Sr. It is also verified that Rb starts appearing at a filament current of 1.15 A (960 K) and disappears completely at 2.1 A, after 3 hours. The other possible isotope that could interfere with ^{90}Sr measurement is [90]Zr. At this filament current of 2.6 A, Zr does not appear in the mass spectrum (as shown in Fig.2), as its enthalpy of vaporization is 3.7 times higher than that of Sr and the corresponding vapour pressure is lower by thirteen orders of magnitude; furthermore the IE of Zr (6.63 eV) also does not favor Zr to form ions at this filament temperature. It is also verified that no Zr[+] could be observed even at 3.5 A (1750 K).

The dissolver solutions obtained from spent fuel of uranium plutonium mixed oxide (MOX) discharged from FBTR is taken for analysis. The fuel is having a composition of $(U_{0.71}Pu_{0.29})O_2$, with 53.5% enriched [233]U in total uranium was irradiated in FBTR and discharged eleven years back, after a burn-up of 108 GWd per ton. The concentration of Cs and Sr in dissolver solutions were measured by an isotope dilution mass spectrometric (IDMS) method. In this method, a known amount of dissolver solution was mixed with a required amount of internal standard (spike) and this homogeneously mixed solution was used for concentration determination. In the present study, [133]Cs with 100% natural abundance and enriched [86]Sr having following isotopic compositions, [84]Sr (0.01%), [86]Sr (95.23%), [87]Sr (0.84%), and [88]Sr (3.92%) were used as spikes. The concentration of Cs and Sr in dissolver solution was calculated using an IDMS equation as follows:

$$C_S = \frac{C_{Sp}W_{Sp}}{W_S} \times \left(\frac{R_{(i/j)Mix} - R_{(i/j)Sp}}{R_{(i/j)S} - R_{(i/j)Mix}} \times R_{(i/j)Sp} \right) \times \frac{\langle AF_{j,Sp} \rangle}{\langle AF_{i,S} \rangle} \times \frac{(AW)_S}{(AW)_{Sp}}$$

where C_{Sp} is the concentration of spike, W_{Sp} the weight of spike, W_S the weight of the sample, $\langle AF_{i,S} \rangle$ and $\langle AF_{j,Sp} \rangle$ the atom fractions of
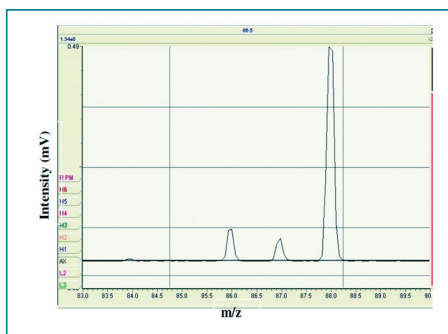
Fig. 2 Mass spectrum of Sr obtained at a filament current of 2.6 A; no interference from Rb and Zr.
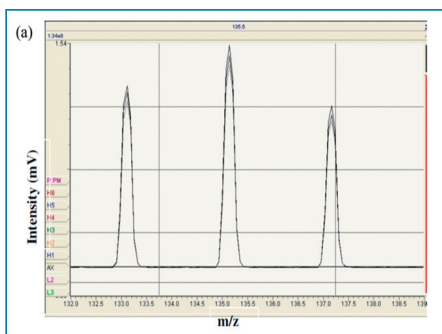
Fig. 3 Mass spectrum of the isotopes of Cs observed from the MOX sample at a filament current of 1.3 A.
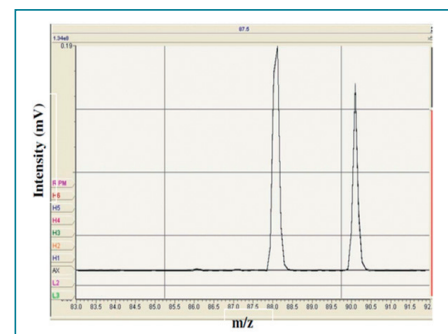
Fig. 4 Mass spectrum of the MOX sample at 2.6 A, showing the presence of Sr isotopes without contribution from isotopes of Zr and Rb.

isotopes i and j in the sample and spike, respectively, $(AW)_S$ and $(AW)_{Sp}$ the average atomic weights of the sample and spike, respectively and $R_{(i/j)S}$, $R_{(i/j)Sp}$ and $R_{(i/j)Mix}$ the ratio of isotopes j and i in the sample, spike, and mixture solutions, respectively. The total elemental concentration of Cs in dissolver solutions was deduced using two ratios of tracers, namely, 135/133 and 137/133; similarly, for the determination of the concentration of Sr, the tracer ratios used were: 86/88 and 90/88. From the total elemental concentration of Cs and Sr, the isotopic concentrations of ^{135}Cs, ^{137}Cs and ^{90}Sr were derived. Fig. 3 shows the mass spectrum of isotopes of Cs observed in MOX sample (obtained at a filament current of 1.3A/1000 K) wherein Ba is completely absent. On increasing the current to 1.5 A (1080 K), the intensity of Cs comes down faster.

On further increasing the current to 2.6 A (1450 K), the mass spectrum obtained covering isotopes of Sr present in the same MOX

Table 2 Concentration of total Sr and ^{90}Sr present in MOX dissolver solution				
	Concentration of Sr (mg g-1)		Concentration of ^{90}Sr (mg g-1)	
Isotope ratio used	86/88	90/88	86/88	90/88
MOX dissolver solution	2107.26 ± 0.70	2032.49 ± 1.29	1004.98 ± 0.33	969.32 ± 0.62

MOX is 6218±4 mg g-1 of the solution. Of this, ^{135}Cs and ^{137}Cs concentrations are 2449±1 mg g-1 and 1729±1mg g-1, respectively. Similarly, data obtained for ^{88}Sr and ^{90}Sr in the dissolver sample is shown in Table 2.

As can be seen from this table, for MOX the total concentrations of Sr obtained by using two different isotope ratios, namely, 86/88 and 90/88 differ by 3.6%. However, it is to be noted that the intensity value obtained for ^{86}Sr is a too small value, having a large error bar.

Table 1 Concentration of total Cs, ^{135}Cs and ^{137}Cs present in MOX dissolver solution					
	Concentration of Cs (mg g-1)		Concentration of ^{135}Cs (mg g-1)		Concentration of 137Cs (mg g-1)
Isotope ratio used	135/133	137/133	135/133	137/133	135/133	137/133
MOX dissolver solution	6220.08 ± 1.04	6216.61 ± 3.50	2449.58 ± 0.41	2448.21 ± 1.38	1729.77 ± 0.29	1728.80 ± 0.97

sample filament, is shown in Fig. 4 (that is, in the same filament that was earlier analyzed for Cs and subsequently maintained at 2.1 A for about 3 h). As can be seen, the intensity at mass 85 amu (expected due to ^{85}Rb) is the same as that of the background, thereby clearly indicating that there is no possible isobaric interference due to ^{87}Rb in the measurement of ^{87}Sr.

From the isotopic ratios and total elemental concentration, the individual isotopic concentration present in the MOX dissolver solution is derived and the values obtained for Cs are shown in Table 1. As can be seen from this table, the concentrations of Cs obtained by using two different isotope ratios (namely, 135/133 and 137/133) differ only by 0.1%. Total Cs concentrations present in

Hence, the values obtained using 90/88 will be more reliable and taken for consideration. The total Sr concentrations are about 2032 ±1mg g-1 of the solution. Of this, ^{90}Sr concentration is 969±0.6 mg g-1 of solution.

Thus, the above study established the assay of ^{135}Cs, ^{137}Cs and ^{90}Sr present in MOX dissolver solution without prior chemical separation, with good precision and accuracy, thereby avoiding labor intensive chemical separation processes, leading to reduction in waste generation and radiation exposure to the personnel.

Internal review meeting on
'Role of Defects in Condensed Matter - Vistas from Materials Science Group'
November 16-17, 2022.

Participants while meeting being conducted at (a, b) e-learning studio and (c) CMPL meeting room. (d) Group photograph in front of CMPL building.

A two-day internal review meeting on 'Role of Defects in Condensed Matter- Vistas from Materials Science Group' was conducted during 16-17 November 2022 in hybrid mode. Dr. N. V. Chandra Shekar, Associate Director, MSG, delivered the welcome address. He highlighted both positive and negative impact of defects on material properties and emphasized the seminal contributions on defects-studies related to reactor materials from MSG. The inaugural address was given by Dr. R. Divakar, Director, Materials Science Group. He discussed significance and relevance of research on defects in nuclear structural materials and its implication to DAE.

The review meeting comprised of an introductory lecture by Dr. R Govindaraj and 10 invited review talks by members of MSG. Dr. Govindaraj recalled the pioneering achievements from MSG on experimental and modelling studies on various fuel and reactor materials. He reviewed the current status of research on defects in condensed matter. The first review talk was delivered by Dr. B. Sundaravel who gave a detailed overview on creating defects in a controlled manner by utilizing 1.7 MV tandetron accelerator, 150 keV and 400 keV accelerators. He also brought out the scope and utility of recently developed dual ion beam line for co-implantation studies. In addition, he also discussed a detailed introduction to the physics of the ion beam implantation and gave a flavor of various ion beam implantation-based experimental techniques to study and characterize defects. These techniques include RBS, ion channeling, NRA, ERDA, PIXE, EELS etc. In specific, he elucidated the work carried out on D9 steels to study the void swelling behaviour using a combination of step height, positron beam based Doppler broadening measurements, the

results of which were corroborated from TEM measurements. The characterization of defects was further carried forward by Dr. S. Abhaya. She highlighted the concepts of characterizing various defects by utilizing positron annihilation spectroscopy. She focused on the recent research works carried out in the lab bringing out the sensitivity and selectivity of positrons to vacancy defects starting from Indian Reduced Activation Ferritic Martensitic steels to nano-porous gold to topological insulators to polymer blends and finally to the iron phosphate glasses. The review then moved onto discussion on defects in nuclear materials. Dr. S. Amirthapandian focused on this and gave a complete overview of the radiation resistance in oxide dispersed strengthened steels giving supporting evidence for the nature of dispersoids present and their kinetics using high resolution TEM images, selected area diffraction etc. The afternoon session was fully dedicated to computer simulations of defects on different scales. First talk by Dr. Gurpreet Kaur gave insights to the solute atoms interactions and binding in Y-Ti, Al and Zr-based ODS steels from first-principles density functional theory (DFT). Dr Ravi Chinnapan talked about the importance of defect calculations from DFT and gave an overview of solute and defect energies in bcc Fe and U. The last talk of the day was delivered by Dr. Manan Dholakia. He gave a review of

molecular dynamics simulations of different defects and study of cascade in single crystal, bicrystal and nanocluster embedded in a matrix of bcc Fe.

The second day started with a detailed presentation by Dr. R. M. Sarguna on bulk synthesis and defect mitigation in technologically important bulk single crystals for radiation detector applications. Dr. Edward Prabu highlighted the role of defects and disorder in superconductors and topological insulators with emphasis on magnetotransport properties. Dr. Kishore Madapu presented a thorough review on defects in 2D semiconducting materials with respect to their role in tuning electronic, optical and magnetic properties. The final presentation of the meeting was by Dr. K. Gururaj who spoke about quantum computers and importance of decoherence time of quantum states and research towards Nitrogen vacancy centers in diamond for usage as qubits. Dr. N. V. Chandra Shekar summarized the talks delivered in the review meeting and concluded by thanking the speakers and the participants.

Reported by
Dr. N. V. Chandra Shekar,
Materials Science Group

Awards, Honours and Recognitions

Dr. John Philip has been appointed as Associate Editor of Hybrid advances of Elsevier Publishers.

Dr. M. Vasudevan has been selected for Fellow of Indian Institute of Metals (FIIM).

Dr. M. Vasudevan is selected as an Editorial Board Member of Engineering Failure Analysis Journal of Elsevier Publishers.

Smt. S. Rajeswari, SIRD, IGCAR is selected as a member of Library Advisory Board of Institute of Physics Publishing, UK, IOPP from 2022.

Best Paper Award

Dr. B. B. Lahiri,
Young Achiever Award in the 66th DAE Solid State Physics Symposium (DAE-SSPS 2022).

M. Vasudevan along with co-authors (D. K. Dwivedi of IIT Roorkee and   Anup Kulkarni of Pratt and Whitney) received the W. H. Hobart Memorial Award 2021 of the American National Welding Society for the paper titled "A functionally graded joint between P91 steel and AISI 316L SS"

Bio-diversity @ DAE Campus, Kalpakkam

Jacobin cuckoo

Jacobin cuckoo formerly known as pied crested cuckoo is black and white in colour with crest. It has a prominent white tip to tail feathers and white patch at the bare of primary feathers. Mostly seen single in wooden countryside.